Advances in Nano Research, *Vol. 14, No.1 (2023) 1-15*
https://doi.org/10.12989/anr.2023.14.1.001

Electronic properties of graphene nanoribbons with Stone-Wales defects using the tight-binding method

M.W. Chuan, S.Z. Lok, A. Hamzah, N.E. Alias, S. Mohamed Sultan, C.S. Lim and M.L.P Tan*

Faculty of Electrical Engineering Engineering, Universiti Teknologi Malaysia, 81310 Skudai, Johor, Malaysia

(*Received August 4, 2021, Revised October 5, 2022, Accepted October 13, 2022*)

Abstract. Driven by the scaling down of transistor node technology, graphene became of interest to many researchers following the success of its fabrication as graphene nanoribbons (GNRs). However, during the fabrication of GNRs, it is not uncommon to have defects within the GNR structures. Scaling down node technology also changes the modelling approach from the classical Boltzmann transport equation to the quantum transport theory because the quantum confinement effects become significant at sub-10 nanometer dimensions. The aim of this study is to examine the effect of Stone-Wales defects on the electronic properties of GNRs using a tight-binding model, based on Non-Equilibrium Green's Function (NEGF) via numeric computation methods using MATLAB. Armchair and zigzag edge defects are also implemented in the GNR structures to mimic the practical fabrication process. Electronic properties of pristine and defected GNRs of various lengths and widths were computed, including their band structure and density of states (DOS). The results show that Stone-Wales defects cause fluctuation in the band structure and increase the bandgap values for both armchair GNRs (AGNRs) and zigzag GNRs (ZGNRs) at every simulated width. In addition, Stone-Wales defects reduce the numerical computation DOS for both AGNRs and ZGNRs. However, when the lengths of the structures increase with fixed widths, the effect of the Stone-Wales defects become less significant.

Keywords: AGNR; band structure; Green's Function DOS; Stone-Wales defect; ZGNR

1. Introduction

The 6-inch single crystallite graphene wafer on copper/ nickel was finally manufactured in 2019 using a Cu/Ni (111) film at 750 °C via chemical vapour deposition (Zhang *et al*. 2019). As a result, research on graphene has become more significant. In addition, the scaling down of node technology has led to the study of graphene nanoribbons (GNRs). In 2020, node technology has achieved sizes as small as 5 nm (Hook 2018) and is in progress to reach 3 nm. Although silicon still dominates the semiconductor market (Chuan *et al*. 2021b), many researchers worried that silicon is unable to go further and therefore have started to research new materials to replace silicon to fulfil Moore's law (Leiserson *et al*. 2020). GNR is a one-dimensional material that confines electrons to movement in only one direction, with reduced scattering processes.

In practice, the edge structure of GNRs can be divided into armchair GNRs (AGNRs) or zigzag GNRs (ZGNRs) (Terrones *et al*. 2010). Since node technology is scaling smaller, quantum transport theory, which uses a bottom-up approach to consider the individual effect of constituent atoms, is applied. The quantum transport model is based on Schrödinger's equation (Schrödinger 1926), which preserves the characteristics of waves of electrons due to its inherent wavefunction in the equation itself. Semiclassical theory, that is, the Boltzmann transport equation (BTE) is no longer suitable for application because it is derived from the drift-diffusion model to solve for the electrical characteristics of devices where the average electron mobilities are calculated as a whole for a particular system. BTE treats electrons as classical particles. Therefore, the most suitable method to be used for nanomaterials (such as 2D graphene) is quantum transport theory because this theory considers the quantum confinement effect, which reduces the effective dimension in which electrons can travel and is hence termed low-dimensional.

During the fabrication of graphene nanoribbons (GNRs), some unavoidable defects occur within the structure. One of the common defects is the Stone-Wales defect. Stone-Wales defects are widely observed in graphene, and hence, their influence on the natural frequencies should be considered in practical applications. By rotating a carbon–carbon bond at 90° within four neighbouring hexagons, the Stone-Wales defects can be created, resulting in the configuration of two pentagons and two heptagons, as shown in Fig. 1 (Terrones *et al*. 2010).

There are 3 assumptions applied during the modelling of graphene nanoribbons (GNRs) with Stone-Wales defect. The first assumption is a basic function that involves the 1s orbital of the hydrogen atom as the basis function to model the structure. The second assumption is solely focused on the interaction between nearest neighbour atoms and ignores the interparticle force. The third assumption is the discretization of the Hamiltonian matrix. With these 3 assumptions, the whole structure becomes a 1D matrix. Solving Schrödinger's equations using first principles or semiempirical methods yield the most basic quantum transport models, such as the non-equilibrium Green's

*Corresponding author, Ph.D.,
E-mail: michael@utm.my

ISSN: 2287-237X (Print), 2287-2388 (Online)

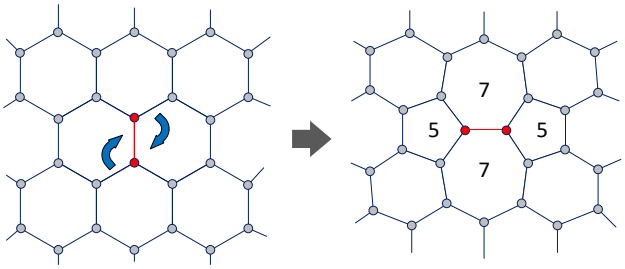

Fig. 1 Schematic diagram showing the formation of a Stone-Wales defect. The defect occurs when the carbon-carbon bond rotates 90° within four neighbouring hexagons to form the Stone-Wales structure (Terrones *et al*. 2010)

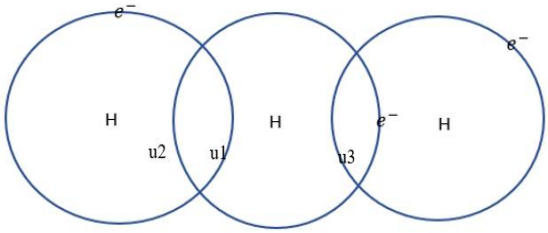

Fig. 2 A 3 hydrogen system, side-by-side with 1s orbital wavefunction

function (NEGF) formalism (Datta 2002) and the Usuki method (Usuki *et al*. 1994, 1995). The Hamiltonian operator, H, the Schrödinger's equation (Eq. (1)) represents the physical system (Baggott 2000), such as the positions of the constituent particles and the interactions between the atoms. Once it is constructed and paired with a suitable wave-function ψ, it can be used to estimate the available energy spectra (Oxtoby *et al*. 2015) that can exist for a particular system, and from there, the electronic properties of the device. Mathematically, the wavefunction of Schrödinger's equation acts as the eigenfunction with the Hamiltonian operator, which contains the eigenvalues that correspond to the allowable quantum energy states. The challenge for constructing a Hamiltonian operator is that it must be simple, easily scalable by size, and accurate enough to be used to hold the correct electrical properties, such as the sub-band structure and density of states (DOS) of the modelled device. The time-independent Schrödinger's equation is written as

$$E\{\psi\} = [H]\{\psi\} \quad (1)$$

discretization of Schrödinger's equation into matrix form, allows faster analysis via computational methods, as it is a powerful tool to solve matrices yielding their corresponding energy eigenvalues.

According to Pauli's exclusion principle, when the numbers of energy states and occupied energy states are known, the number of carriers can be determined. The number of energy states represents the density of state (DOS), and the occupied energy states are Fermi-Dirac distributions. By multiplying both terms, the number of carriers for the material can be known and used for further analysis. This shows how important this work is to determine the DOS of certain materials. The band structure of the material, which shows the intrinsic properties of the material, is visualized by the summation of all allowable energy levels at k-points corresponding to a given momentum. In addition to the intrinsic properties, the minimum bandgap values can also be known from the difference between the conduction band and valence band of the visualized band structure. From there, the material type can be determined to be metallic, insulator or semiconductor.

In recent studies, machine learning (ML) and density-functional tight-binding (DFTB) are used to predict complex material properties with better accuracy than density functional theory (DFT) and first-principal calculation up to 1000 atoms (Lee *et al*. 2018, Kurban *et al*. 2021a, b, Kurban and Kurban 2021). In this work, numeric computation using MATLAB is also able to produce more efficient results than the computationally expensive DFT and first-principle calculation. In this paper, a semi-empirical model based on a tight-binding approach is applied to study the effect of Stone-Wales defects on the electronic properties, such as the band structure and density of state (DOS), of graphene nanoribbons (GNRs). In Section 2, a literature review on Stone-Wales defects is presented, and the modelling of Stone-Wales defects into a Hamiltonian matrix is also discussed in this section. In Section 3, the mathematical modelling of the band structure and density of states (DOS) using the nearest neighbour tight-binding (NNTB) approach are shown. In Section 4, the simulated results, such as the band structure and density of state (DOS), from MATLAB are shown and analysed. Finally, in Section 5, a conclusion is presented based on the findings of this work.

2. Related research

Goh *et al*. (2018) discussed the process of modelling GNRs using 3 simplifying assumptions based on Hartree's assumption and presented the MATLAB script used to compute the electronic properties. Their study paper provides simple yet accurate information to help readers understand how to model on GNR. The assumptions used to simplify or transform many electron wavefunctions to single electron wavefunctions can change the Hamiltonian operator to a matrix of 1D structure. This eases the modelling for GNRs with Stone-Wales defects. The many-electrons wavefunction can be assumed to be just a product of many single-electron problems, also known as Hartree's product. These single-electron wavefunctions can take the form of plane waves with periodic boundary conditions applied in a uniform system. A free hydrogen atom has an electron on its outermost orbital, and the wavefunction of the hydrogen 1s electron orbital is applied as the basis function to model the system. Extending this concept to a larger problem, in a multilevel orbital system, such as a 2D graphene sheet, although it has 2 shells, only the π-electron of the $2p_z$ orbital and its respective wavefunction are being considered as the basis function. Based on Fig. 2, the second important simplifying assumption that can be made is that the wavefunction of 1s orbitals only overlaps with another orbital directly adjacent to it. This is an important criterion that will be used throughout this entire study, in

which only the interaction of single nearest neighbour tight-binding (Reich *et al*. 2008) energy is considered and other interparticle forces are ignored.

The third simplifying assumption will involve the Hamiltonian operator. With the first simplifying assumption which is the basic function, the Hamiltonian operator can be discretized into matrix form. This will ease the modelling process in which computational methods through powerful matrix tools are used to solve the energy spectrum of the device. This can be justified because the structure lattice itself is made up of discrete atoms at the atomic level. With all the simplifying assumptions applied, the Hamiltonian matrix which is the core of the whole project, can be shown below as Eq. (2). The following equation is using a three-hydrogen atom as an example, with u1, u2 and u3 being the 1s orbital potential function.

$$E\begin{Bmatrix}\varphi_1\\ \varphi_2\\ \varphi_3\end{Bmatrix}=\begin{bmatrix}u_{11} & u_{12} & 0\\ u_{21} & u_{22} & u_{23}\\ 0 & u_{32} & u_{33}\end{bmatrix}\begin{Bmatrix}\varphi_1\\ \varphi_2\\ \varphi_3\end{Bmatrix} \quad (2)$$

In real or practical modelling of devices, the terms along the diagonal represent the self-interacting energies. In this example, it will be effectively 0 because the 1s orbital electron does not have any interactions with itself. u_{12}, u_{21}, u_{23}, and u_{32} are the interacting energies between nearest neighbour atoms, and the energies are the same since they are from the same orbital electron of the same atom. u_{13} and u_{31} are simply 0 by following the second simplifying assumption where no interaction between nearest neighbouring atoms, indicating no is energy present. In this study, all the terms will be expressed in terms of t, which represent the tight-binding energy and is obtained from other well-developed research. Therefore, Schrödinger's equation is solved semi-empirically. Chang *et al*. (2013) studied the effect of vacancies and defects, providing the Stone-Wales structure that was used in this study, and its simulated results act as a benchmark of the project for the band structure of Armchair GNRs (AGNRs). For zigzag GNRs (ZGNRs), the benchmark is based on research nu Faez and Barami (2013) on the spin effect of Stone-Wales AGNRs and ZGNRs. They compared the Stone-Wales AGNRs and ZGNRs with and without the spin effects. The simulated band structure for Stone-Wales ZGNRs and Stone-Wales AGNRs without the spin effect is used as the benchmark. Stone-Wales defect affected DOS and the band structure of other materials, such as hexagonal boron nitride in the study by Hamdi *et al*. (2020), providing an additional reference for this work for the observation on the behaviour of the trends of the band structure and DOS. The trends of the band structure when Stone-Wales defects are applied to pristine graphene were presented by Kumar *et al*. (2020). A previous study on the effects of vacancies and divacancies on the band structure and DOS of AGNRs and ZGNRs was performed by Wong *et al*. (2019), providing a guideline for this work to further investigate the effects of varying the width and length of the GNRs with Stone-Wales effect.

The changes in the geometry of GNRs when Stone-Wales defects are present affect the bond length and thus affect the tight-binding energy. The renormalized tight-binding energy can be determined by a formula proposed by Rodrigues *et al*. (2011), that depends on the bond length of carbon-carbon atoms. The affected bond length for GNRs with Stone-Wales was also studied by Nguyen *et al*. (2018), and we employed the same bond length values in this study. The GNRs with Stone-Wales defect at the centre of the structure changes the interaction energy between carbon-carbon bonds due to changes in the atomic length of some carbon-carbon bonds. The carbon-carbon length is the length after relaxation of the geometry of the atomic structure, and the interaction energy can be obtained based on the length of the carbon-carbon bonds. Buapong and Hanlumyuang (2017) studied the effect of randomly occurring Stone-Wales defects on the mechanical properties of carbon nanotubes using atomistic simulation. From their research, Stone-Wales defects are caused by mechanical strain, which can affect the electronic and mechanical properties of the material according to Zhang *et al*. (2017). This effect can also be proven by studying the effect of strain/stress on the mechanical and electronic properties of phosphorene nanosheets and nanotubes. That study shows that band structures are very sensitive to strain and provides a reference for this experiment. This work extended the MATLAB script for the GNR model that was written by Datta *et al*. (2009) to incorporate and further investigate the effects of the Stone-Wales defects.

3. Mathematical modelling

The most important element in constructing a Hamiltonian matrix will be the unit cell or alpha matrix. The definition of the alpha matrix for Stone-Wales defective GNRs (SWGNRs) in both the armchair and zigzag directions was also studied, and the tight-binding energy was based on the NEGF tight-binding models from Datta (1997), Datta *et al*. (2009), Chin *et al*. (2012), Hawkins *et al*. (2012). The value of 2.7 eV is chosen as the tight-binding energy for neighbouring $2p_z$ π-orbital of the carbon atoms. The beta matrix is the interaction between the unit cell or alpha matrices. The width of the AGNR can be determined by the number of atoms in the x-direction, and the length depends on the number of unit cells, as shown in Fig. 3. The numbering of the unit cell is in the clockwise direction for AGNRs. For example, in Fig. 3, for unit cell number 1, the numbering starts at A1 and runs to A14 in the clockwise direction. However, in Fig. 4, for unit cell number 1, the numbering starts at A1 runs to A12, and the numbering follows a zigzag manner. A1 to A14 are the labels for the atoms, and the bonds. For example, between A1 and A2 or A1 and A14 are the tight-binding energies, which are t = 2.7 eV.

The beta matrix is the interaction between nearest neighbouring alpha matrices. The Hamiltonian matrix constructed of alpha matrices and beta matrices. Once the alpha and beta matrices are defined, the Hamiltonian matrix is used in the MATLAB script to generate the band structure and DOS of the material. The MATLAB function 'kron' is used to generate the Hamiltonian matrix based on defined alpha and beta matrices. The tight-binding energy, width, and length will be the input for the MATLAB script to

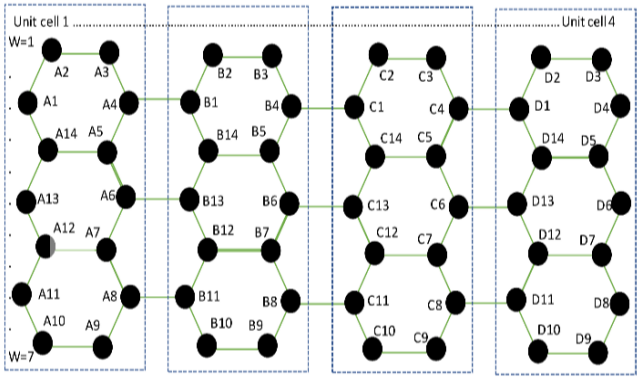

Fig. 3 AGNR with length=4 with 4-unit cells and 7 atoms in a single row represents a width of 7

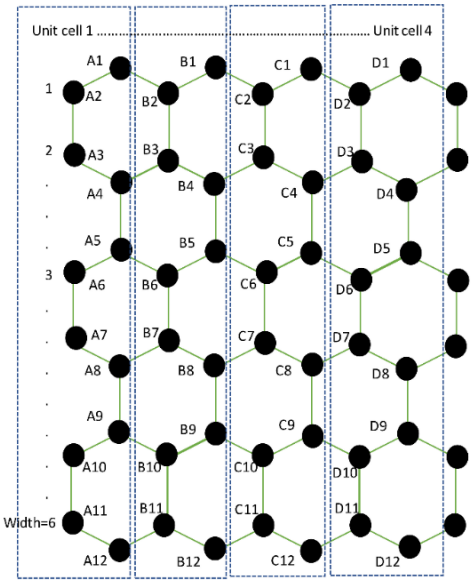

Fig. 4 ZGNR with length=4 with 4-unit cells and 6 atoms in a single row represents a width of 6

determine the Hamiltonian matrix. The final Hamiltonian matrix can be presented as in Eq. (3).

$$H = \begin{bmatrix} \alpha & \beta & 0 \\ \beta' & \alpha & \beta \\ 0 & \beta' & \alpha \end{bmatrix} \tag{3}$$

The normalized tight-binding energy will depend on the length of the carbon-carbon bond. The shorter the bond, the higher the tight-binding energy compared to the normal or pristine length, which is 1.42 Å, and 2.7 eV is the tight-binding energy (Wang *et al*. 2008). The structure or geometry of pristine GNRs changes when Stone-Wales defects are implemented. The lengths between carbon-carbon will vary and, as a result, change the interaction energy between the carbon-carbon bonds. The tight-binding energy for the affected length will also be required to vary to improve the accuracy of the result. Eq. (4) (Rodrigues *et al*. 2011) is used to determine the new tight-binding energy of the affected bond.

$$\tau(r_{ij}) = (\frac{r_{ij}}{\alpha_0})^{-\alpha_2} \, exp\,[-\alpha_3 * (r_{ij}{}^{\alpha_4} - \alpha_0{}^{\alpha_4})] \tag{4}$$

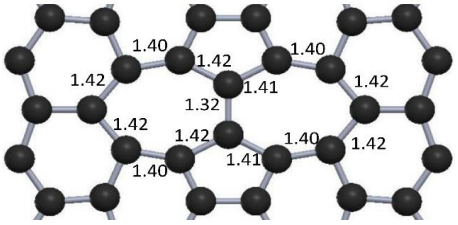

(a)

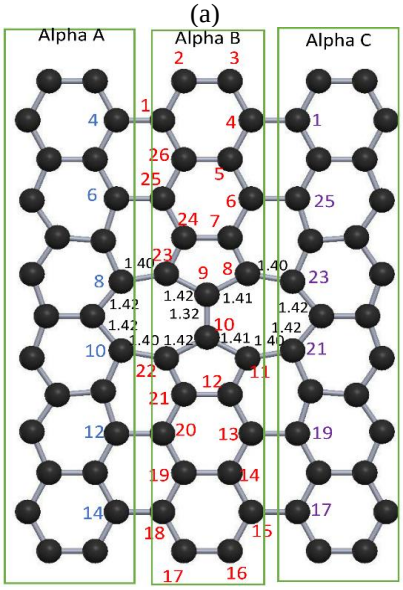

(b)

Fig. 5 (a) AGNR bond length (Nguyen *et al*. 2018) and (b) corresponding position of the 13-AGNR, L=3 (Chang *et al*. 2013)

Table 1 The renormalised tight-binding energies corresponding to different bond lengths

Bond length (Å)	New hopping amplitude	New tight-binding energy (eV)
1.32	1.2172*t	3.28644
1.40	1.0411*t	2.81097
1.41	1.0204*t	2.75508
1.42	t	2.70000

where α_0 is the carbon-carbon distance in the bulk (in units of angstroms), α_0 =1.42 Å, while r_{ij} represents the distance between the carbons labelled i and j (given in units of angstroms) or the carbon-carbon bond length. The parameters obtained from fitting are as follows: α_2 =1.2785, α_3 =0.1383, and α_4 = 3.4490 (Tang *et al*. 1996). The resulting τ is hopping amplitudes, and τ is expressed in terms of t to represents the renormalized tight-binding energies.

The geometry of pristine AGNRs and ZGNRs changed due to the presence of Stone-Wales defects. Therefore, tight-binding at t = 2.7 eV required renormalisation to adapt to the changes in energy between the carbon-carbon bonds. By using Eq. (4) and the length given by (Chang *et al*., 2013) as shown in Fig. 5, the new value of tight-binding energies are tabulated in Table 1. The bond length and the tight-binding energy for the unaffected carbon-carbon bonds are maintained as 1.42 Å and 2.7 eV, respectively.

$$\alpha_A = \begin{bmatrix}
0 & t & 0 & 0 & 0 & 0 & 0 & 0 & 0 & 0 & 0 & 0 & \dots & 0 & 0 & 0 & 0 & t \\
t & 0 & t & 0 & 0 & 0 & 0 & 0 & 0 & 0 & 0 & 0 & \dots & 0 & 0 & 0 & 0 & 0 \\
0 & t & 0 & t & 0 & 0 & 0 & 0 & 0 & 0 & 0 & 0 & \dots & 0 & 0 & 0 & 0 & 0 \\
0 & 0 & t & 0 & t & 0 & 0 & 0 & 0 & 0 & 0 & 0 & \dots & 0 & 0 & 0 & 0 & 0 \\
0 & 0 & 0 & t & 0 & t & 0 & 0 & 0 & 0 & 0 & 0 & \dots & 0 & 0 & 0 & 0 & t \\
0 & 0 & 0 & 0 & t & 0 & t & 0 & 0 & 0 & 0 & 0 & \dots & 0 & 0 & 0 & 0 & 0 \\
0 & 0 & 0 & 0 & 0 & t & 0 & t & 0 & 0 & 0 & 0 & \dots & 0 & 0 & t & 0 & 0 \\
0 & 0 & 0 & 0 & 0 & 0 & t & 0 & t & 0 & 0 & 0 & \dots & 0 & 0 & 0 & 0 & 0 \\
0 & 0 & 0 & 0 & 0 & 0 & 0 & t & 0 & t & 0 & 0 & \dots & t & 0 & 0 & 0 & 0 \\
0 & 0 & 0 & 0 & 0 & 0 & 0 & 0 & t & 0 & t & 0 & \dots & 0 & 0 & 0 & 0 & 0 \\
0 & 0 & 0 & 0 & 0 & 0 & 0 & 0 & 0 & t & 0 & t & \dots & 0 & 0 & 0 & 0 & 0 \\
0 & 0 & 0 & 0 & 0 & 0 & 0 & 0 & 0 & 0 & t & 0 & \ddots & 0 & 0 & 0 & 0 & 0 \\
\vdots & \vdots & \vdots & \vdots & \vdots & \vdots & \vdots & \vdots & \vdots & \vdots & \vdots & \ddots & \ddots & \ddots & \vdots & \vdots & \vdots & \vdots \\
0 & 0 & 0 & 0 & 0 & 0 & 0 & 0 & t & 0 & 0 & 0 & \ddots & 0 & t & 0 & 0 & 0 \\
0 & 0 & 0 & 0 & 0 & 0 & 0 & 0 & 0 & 0 & 0 & 0 & \dots & t & 0 & t & 0 & 0 \\
0 & 0 & 0 & 0 & 0 & 0 & t & 0 & 0 & 0 & 0 & 0 & \dots & 0 & t & 0 & t & 0 \\
0 & 0 & 0 & 0 & 0 & 0 & 0 & 0 & 0 & 0 & 0 & 0 & \dots & 0 & 0 & t & 0 & t \\
t & 0 & 0 & 0 & t & 0 & 0 & 0 & 0 & 0 & 0 & 0 & \dots & 0 & 0 & 0 & t & 0
\end{bmatrix} \tag{5}$$

$$\alpha_B = \begin{bmatrix}
0 & t & 0 & 0 & 0 & 0 & 0 & 0 & 0 & 0 & 0 & 0 & \dots & 0 & 0 & 0 & 0 & t \\
t & 0 & t & 0 & 0 & 0 & 0 & 0 & 0 & 0 & 0 & 0 & \dots & 0 & 0 & 0 & 0 & 0 \\
0 & t & 0 & t & 0 & 0 & 0 & 0 & 0 & 0 & 0 & 0 & \dots & 0 & 0 & 0 & 0 & 0 \\
0 & 0 & t & 0 & t & 0 & 0 & 0 & 0 & 0 & 0 & 0 & \dots & 0 & 0 & 0 & 0 & 0 \\
0 & 0 & 0 & t & 0 & t & 0 & 0 & 0 & 0 & 0 & 0 & \dots & 0 & 0 & 0 & 0 & t \\
0 & 0 & 0 & 0 & t & 0 & t & 0 & 0 & 0 & 0 & 0 & \dots & 0 & 0 & 0 & 0 & 0 \\
0 & 0 & 0 & 0 & 0 & t & 0 & t & 0 & 0 & 0 & 0 & \dots & 0 & 0 & t & 0 & 0 \\
0 & 0 & 0 & 0 & 0 & 0 & t & 0 & 1.0204t & 0 & 0 & 0 & \dots & 0 & 0 & 0 & 0 & 0 \\
0 & 0 & 0 & 0 & 0 & 0 & 0 & 1.0204t & 0 & 1.2172t & 0 & 0 & \dots & 0 & t & 0 & 0 & 0 \\
0 & 0 & 0 & 0 & 0 & 0 & 0 & 0 & 1.2172t & 0 & 1.0204t & 0 & \dots & t & 0 & 0 & 0 & 0 \\
0 & 0 & 0 & 0 & 0 & 0 & 0 & 0 & 0 & 1.0204t & 0 & t & \dots & 0 & 0 & 0 & 0 & 0 \\
0 & 0 & 0 & 0 & 0 & 0 & 0 & 0 & 0 & 0 & t & 0 & \ddots & 0 & 0 & 0 & 0 & 0 \\
\vdots & \vdots & \vdots & \vdots & \vdots & \vdots & \vdots & \vdots & \vdots & \vdots & \vdots & \ddots & \ddots & \ddots & \vdots & \vdots & \vdots & \vdots \\
0 & 0 & 0 & 0 & 0 & 0 & 0 & 0 & 0 & t & 0 & 0 & \ddots & 0 & 0 & 0 & 0 & 0 \\
0 & 0 & 0 & 0 & 0 & 0 & 0 & 0 & t & 0 & 0 & 0 & \dots & 0 & 0 & t & 0 & 0 \\
0 & 0 & 0 & 0 & 0 & 0 & t & 0 & 0 & 0 & 0 & 0 & \dots & 0 & t & 0 & t & 0 \\
0 & 0 & 0 & 0 & 0 & 0 & 0 & 0 & 0 & 0 & 0 & 0 & \dots & 0 & 0 & t & 0 & t \\
t & 0 & 0 & 0 & t & 0 & 0 & 0 & 0 & 0 & 0 & 0 & \dots & 0 & 0 & 0 & t & 0
\end{bmatrix} \tag{6}$$

$$\beta_{AB} = \begin{bmatrix}
0 & 0 & \dots & 0 & 0 & 0 & 0 & 0 & 0 & 0 & 0 & 0 & 0 & 0 \\
0 & 0 & \dots & 0 & 0 & 0 & 0 & 0 & 0 & 0 & 0 & 0 & 0 & 0 \\
0 & 0 & \dots & 0 & 0 & 0 & 0 & 0 & 0 & 0 & 0 & 0 & 0 & 0 \\
t & 0 & \dots & 0 & 0 & 0 & 0 & 0 & 0 & 0 & 0 & 0 & 0 & 0 \\
0 & 0 & \dots & 0 & 0 & 0 & 0 & 0 & 0 & 0 & 0 & 0 & 0 & 0 \\
0 & 0 & \dots & 0 & 0 & 0 & 0 & 0 & 0 & 0 & 0 & 0 & t & 0 \\
0 & 0 & \dots & 0 & 0 & 0 & 0 & 0 & 0 & 0 & 0 & 0 & 0 & 0 \\
0 & 0 & \dots & 0 & 0 & 0 & 0 & 0 & 0 & 0 & 1.0411t & 0 & 0 & 0 \\
0 & 0 & \dots & 0 & 0 & 0 & 0 & 0 & 0 & 0 & 0 & 0 & 0 & 0 \\
0 & 0 & \dots & 0 & 0 & 0 & 0 & 0 & 0 & 1.0411t & 0 & 0 & 0 & 0 \\
0 & 0 & \dots & 0 & 0 & 0 & 0 & 0 & 0 & 0 & 0 & 0 & 0 & 0 \\
0 & 0 & \dots & 0 & 0 & 0 & 0 & t & 0 & 0 & 0 & 0 & 0 & 0 \\
0 & 0 & \dots & 0 & 0 & 0 & 0 & 0 & 0 & 0 & 0 & 0 & 0 & 0 \\
0 & 0 & \dots & 0 & 0 & t & 0 & 0 & 0 & 0 & 0 & 0 & 0 & 0 \\
0 & 0 & \dots & 0 & 0 & 0 & 0 & 0 & 0 & 0 & 0 & 0 & 0 & 0 \\
0 & 0 & \dots & 0 & 0 & 0 & 0 & 0 & 0 & 0 & 0 & 0 & 0 & 0 \\
\vdots & \vdots & \ddots & \vdots & \vdots & \vdots & \vdots & \vdots & \vdots & \vdots & \vdots & \vdots & \vdots & \vdots \\
0 & 0 & \dots & 0 & 0 & 0 & 0 & 0 & 0 & 0 & 0 & 0 & 0 & 0 \\
0 & 0 & \dots & 0 & 0 & 0 & 0 & 0 & 0 & 0 & 0 & 0 & 0 & 0
\end{bmatrix} \tag{7}$$

$$\beta_{BC} = \begin{bmatrix} 0 & 0 & \dots & 0 & 0 & 0 & 0 & 0 & 0 & 0 & 0 & 0 & 0 & 0 \\ 0 & 0 & \dots & 0 & 0 & 0 & 0 & 0 & 0 & 0 & 0 & 0 & 0 & 0 \\ 0 & 0 & \dots & 0 & 0 & 0 & 0 & 0 & 0 & 0 & 0 & 0 & 0 & 0 \\ t & 0 & \dots & 0 & 0 & 0 & 0 & 0 & 0 & 0 & 0 & 0 & 0 & 0 \\ 0 & 0 & \dots & 0 & 0 & 0 & 0 & 0 & 0 & 0 & 0 & 0 & 0 & 0 \\ 0 & 0 & \dots & 0 & 0 & 0 & 0 & 0 & 0 & 0 & 0 & t & 0 & 0 \\ 0 & 0 & \dots & 0 & 0 & 0 & 0 & 0 & 0 & 0 & 0 & 0 & 0 & 0 \\ 0 & 0 & \dots & 0 & 0 & 0 & 0 & 0 & 0 & 0 & 1.0411t & 0 & 0 & 0 \\ 0 & 0 & \dots & 0 & 0 & 0 & 0 & 0 & 0 & 0 & 0 & 0 & 0 & 0 \\ 0 & 0 & \dots & 0 & 0 & 0 & 0 & 0 & 0 & 0 & 0 & 0 & 0 & 0 \\ 0 & 0 & \dots & 0 & 0 & 0 & 0 & 0 & 1.0411t & 0 & 0 & 0 & 0 & 0 \\ 0 & 0 & \dots & 0 & 0 & 0 & 0 & 0 & 0 & 0 & 0 & 0 & 0 & 0 \\ 0 & 0 & \dots & 0 & 0 & 0 & t & 0 & 0 & 0 & 0 & 0 & 0 & 0 \\ 0 & 0 & \dots & 0 & 0 & 0 & 0 & 0 & 0 & 0 & 0 & 0 & 0 & 0 \\ 0 & 0 & \dots & 0 & t & 0 & 0 & 0 & 0 & 0 & 0 & 0 & 0 & 0 \\ 0 & 0 & \dots & 0 & 0 & 0 & 0 & 0 & 0 & 0 & 0 & 0 & 0 & 0 \\ \vdots & \vdots & \ddots & \vdots & \vdots & \vdots & \vdots & \vdots & \vdots & \vdots & \vdots & \vdots & \vdots & \vdots \\ 0 & 0 & \dots & 0 & 0 & 0 & 0 & 0 & 0 & 0 & 0 & 0 & 0 & 0 \\ 0 & 0 & \dots & 0 & 0 & 0 & 0 & 0 & 0 & 0 & 0 & 0 & 0 & 0 \end{bmatrix} \quad (8)$$

3.1 Alpha matrix

Table 1 shows the renormalised tight-binding energies corresponding to different carbon-carbon bond lengths. From the table, it is shown that the shorter the bond lengths, the higher the tight-binding energies. There are 3-unit cells shown in Fig. 5 and the numbering is just a reference to show the interaction between the nearest neighbouring carbon atoms. Based on Fig. 5, the alpha matrix A can be shown in Eq. (5). Alpha matrix A and alpha matrix C are the same. Since the Stone-Wales defect only exists at the centre, the affected self-interacting unit cell is alpha matrix B, which can be observed in Eq. (6). All alpha matrices are 26×26 matrices because there are 26 carbon atoms in one unit cell or 2 times the width of the AGNR. Red coloured values are the renormalized tight-binding energies that can be observed within alpha matrix B in Eq. (6).

3.2 Beta matrix

The beta matrices show the interactions of all unit-cell alpha matrices. There are 2 beta matrices since there are 3-unit cells, and they are adjacent to each other. The matrix is 26×26, which is the same as the alpha matrix. The red coloured values represent the renormalised tight-binding energies, which are shown in Eqs. (7) and (8).

3.3 Hamiltonian matrix

The final Hamiltonian matrix will be 78×78 in size after substituting the alpha and beta in Eq. (9). Each alpha and beta matrix is of a size of 26×26; hence, 26 times 3 will be 78 for each column and each row of the final Hamiltonian equation. The MATLAB command 'kron' combines all alpha and beta matrices by applying Eq. (9).

$$H_{13-AGNR,L=3} = \begin{bmatrix} \alpha_A & \beta_{AB} & 0 \\ \beta_{BA} & \alpha_B & \beta_{BC} \\ 0 & \beta_{CB} & \alpha_C \end{bmatrix} \quad (9)$$

By generating the Hamiltonian matrix inside MATLAB based on the method mentioned above, the band structure and DOS can be obtained. Note that β_{BA} and β_{CB} are the transposes of β_{AB} and β_{BC}, respectively. The mathematical modelling for ZGNRs were repeated using the same approach used in AGNRs by using the structure in Fig. 4.

3.4 Band structure calculation

The Hamiltonian matrix in general can be computed as in Eq. (10) using the concept from the previous sections with N being the number of atom chains and ε being the self-interacting energies. Note that the ε represents self-interacting energies. To create periodic boundary conditions, additional bolded **t** terms are added to show that the first atom and N^{th} atom are side-by -side.

$$E\begin{Bmatrix} \varphi_1 \\ \varphi_2 \\ \vdots \\ \varphi_{N-1} \\ \varphi_N \end{Bmatrix} = \begin{bmatrix} \varepsilon & t & 0 & \cdots & & \boldsymbol{t} \\ t & \varepsilon & t & 0 & \cdots & \\ 0 & t & \varepsilon & t & 0 & \cdots \\ & \ddots & \ddots & \ddots & \ddots & \ddots \\ & & \ddots & \ddots & \ddots & \ddots \\ \boldsymbol{t} & & \cdots & 0 & t & \varepsilon \end{bmatrix} \begin{Bmatrix} \varphi_1 \\ \varphi_2 \\ \vdots \\ \varphi_{N-1} \\ \varphi_N \end{Bmatrix} \quad (10)$$

The overall matrix equation can be collapsed into a single linear equation to form Eq. (11) when periodic boundary is applied:

$$E_{\varphi_n} = t_{\varphi_{n-1}} + \varepsilon_{\varphi_n} + t_{\varphi_{n+1}} \quad (11)$$

The wavefunction can be well approximated with a plane wave as in Eq. (12) because the coefficients of the linear matrix equation are always static, effectively transforming it into a function of the wavenumber, k. Dividing the N^{th} minus one wavefunction by the N^{th} wavefunction, Eq. (13) can be obtained:

$$\varphi_n = \varphi_0 e^{+inka} \quad (12)$$

$$\frac{\varphi_{n-1}}{\varphi_n} = \frac{e^{+i(n-1)ka}}{e^{inka}} = e^{-ika} \quad (13)$$

Eq. (13) transforms Eq. (11) into the final dispersion relation, forming Eq. (14), which is applied to compute the

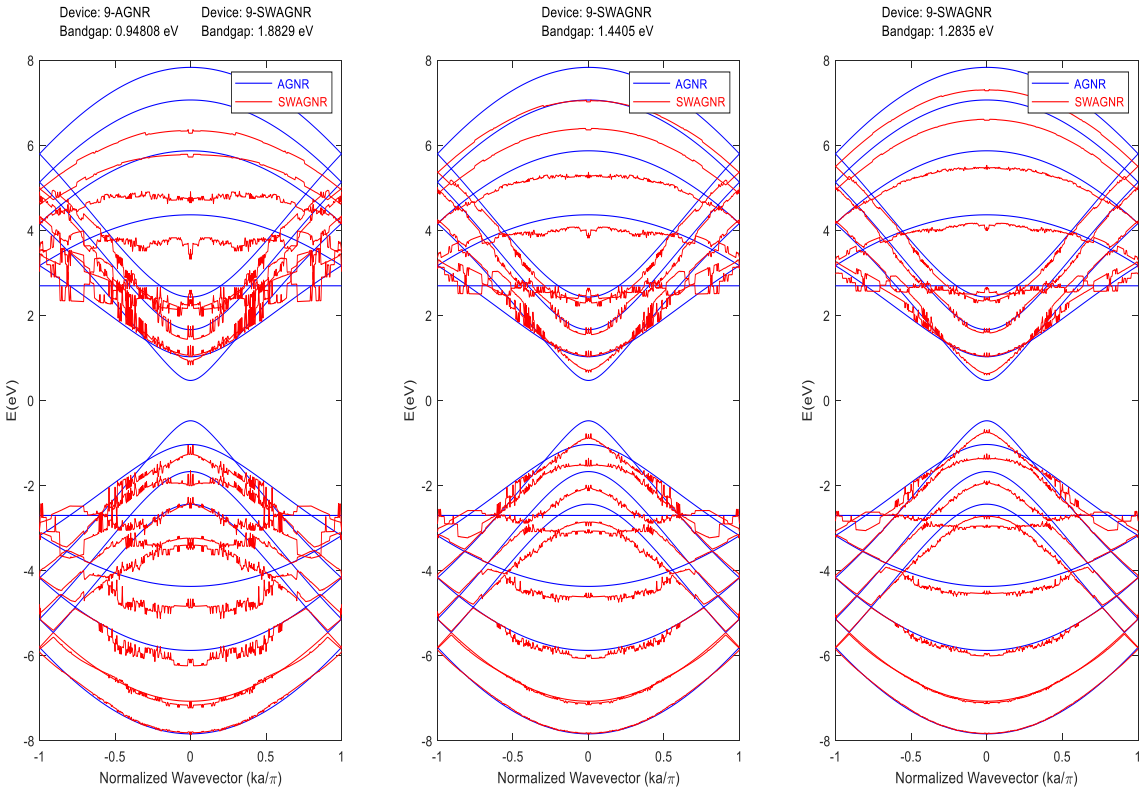

Fig. 6 Band structures of pristine AGNRs (blue) and SW-AGNRs (red) with widths of 9 and different lengths of (a) 11, (b) 21, and (c) 31 unit cells

energy spectrum in this work. The dispersion equation has a canonical form in trigonometric terms, but it will not be utilised in this work.

$$E = te^{-ika} + \varepsilon + te^{+ika} \equiv \varepsilon + 2t\ cos\ (ka) \tag{14}$$

3.5 DOS and Green's Function DOS calculation

The DOS is computed from the band structure of the material. There are several ways to compute the DOS, but one of the easiest ways is to apply the mathematical equation of delta function (Datta 2005). The total DOS of a system with N bands is shown by Eq. (15). N is usually twice the number of electrons involved in the transport per atom of a system. This is because each electron contributes to a conduction-valence subband pair. Using Fig. 2 as an example, 3 hydrogen atoms are present; therefore, 6 bands are present in the subband structure.

$$DOS(E) = \sum_{i=1}^{N} \frac{1}{2\pi} \int \delta[E_i(k) - E]dk \tag{15}$$

The delta function in Eq. (15) is then be replaced by the distribution as in Eq. (16), forming Eq. (17). Since the model in this study has a periodic structure, k values within the first Brillouin zone are sufficient to represent the whole system.

$$\delta[E_i(k) - E] \rightarrow \frac{\eta_G}{[E_i(k) - E]^2 + {\eta_G}^2} \tag{16}$$

$$DOS(E) = \sum_{i=1}^{N} \frac{1}{2\pi} \sum_{all\ k} \frac{\eta_G}{[E_i(k) - E]^2 + {\eta_G}^2} \tag{17}$$

The DOS can also be computed using Green's function (Datta 1997, Li and Lu 2008) through the relation which in Eq. (18), where G_F represents the retarded Green's function as shown in Eq. (19), η is a very small imaginary value to prevent the inverse matrix from diverging, I is an identity matrix, and H is the Hamiltonian operator matrix (Wong *et al*. 2020).

$$DOS(E) = \frac{1}{\pi} Im[Trace(G_F)] \tag{18}$$

$$G^{retarded} = [(E + i\eta) * I - H]^{-1} \tag{19}$$

Both methods are used side by side to compute the DOS for GNRs. Calculation of the DOS via delta function will not have any length information embedded in it, unlike the Green's function method, since the Hamiltonian matrices will capture the full dimension of the modelled structure, including the information of the lengths.

4. Result and discussion

4.1 Band structure of AGNR

Fig. 6 shows the band structure of AGNRs (blue) and Stone-Wales defective AGNRs (red) with widths of 9 and

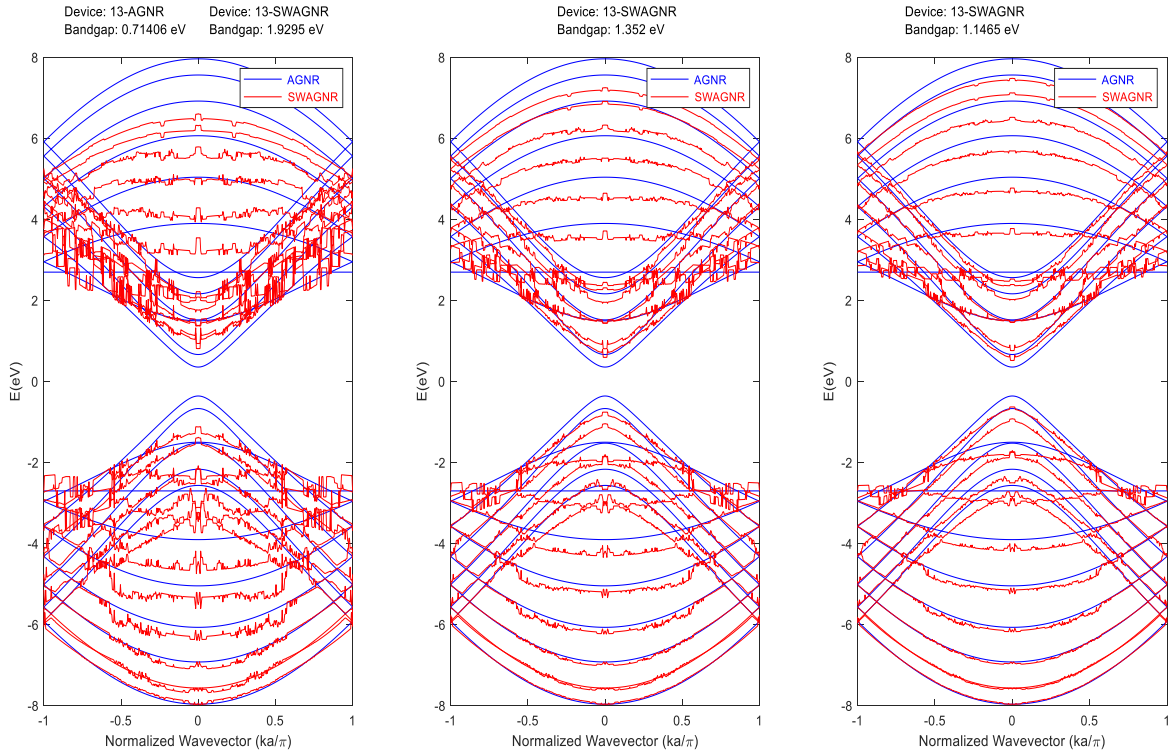

(a) (b) (c)

Fig. 7 Band structures of pristine AGNRs (blue) and SW-AGNRs (red) with widths of 13 and different lengths of (a) 11, (b) 21 and (c) 31 unit cells

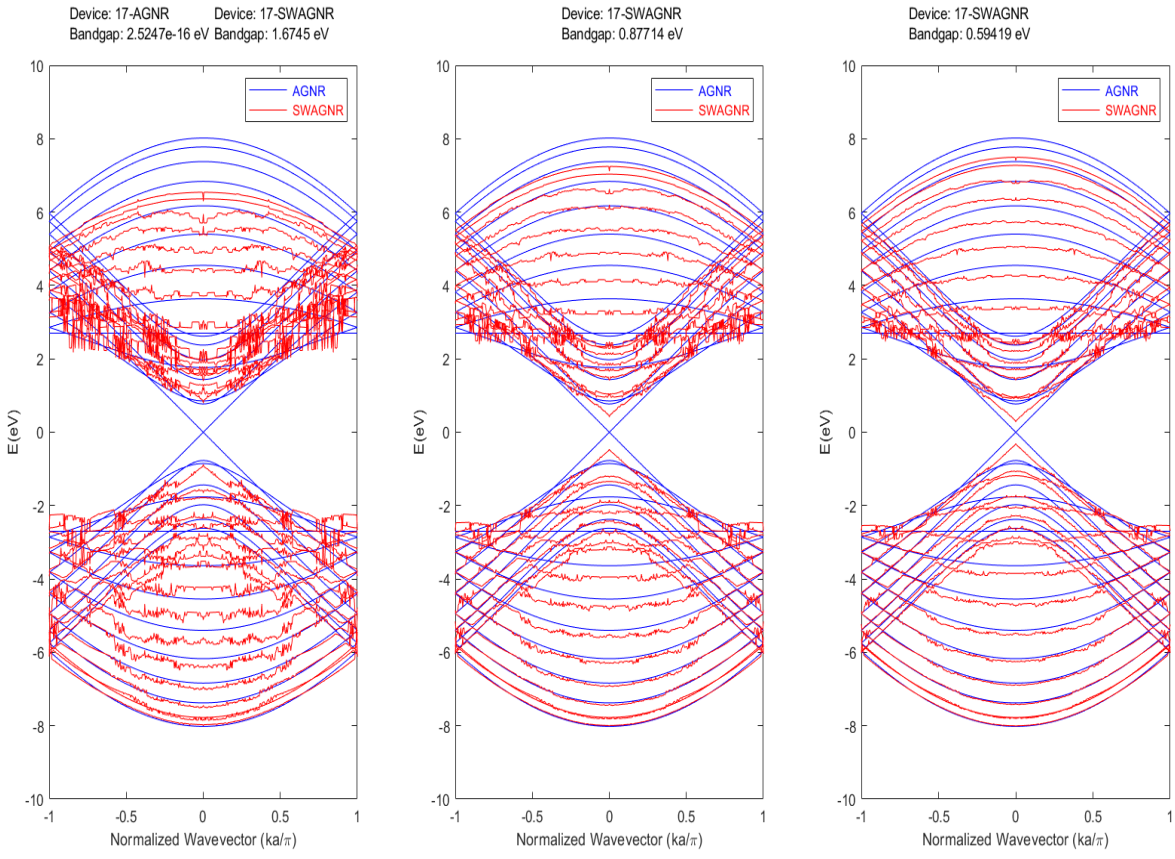

(a) (b) (c)

Fig. 8 Band structures of pristine AGNRs (blue) and SW-AGNRs (red) with widths of 17 and different lengths of (a) 11, (b) 21 and (c) 31 unit cells

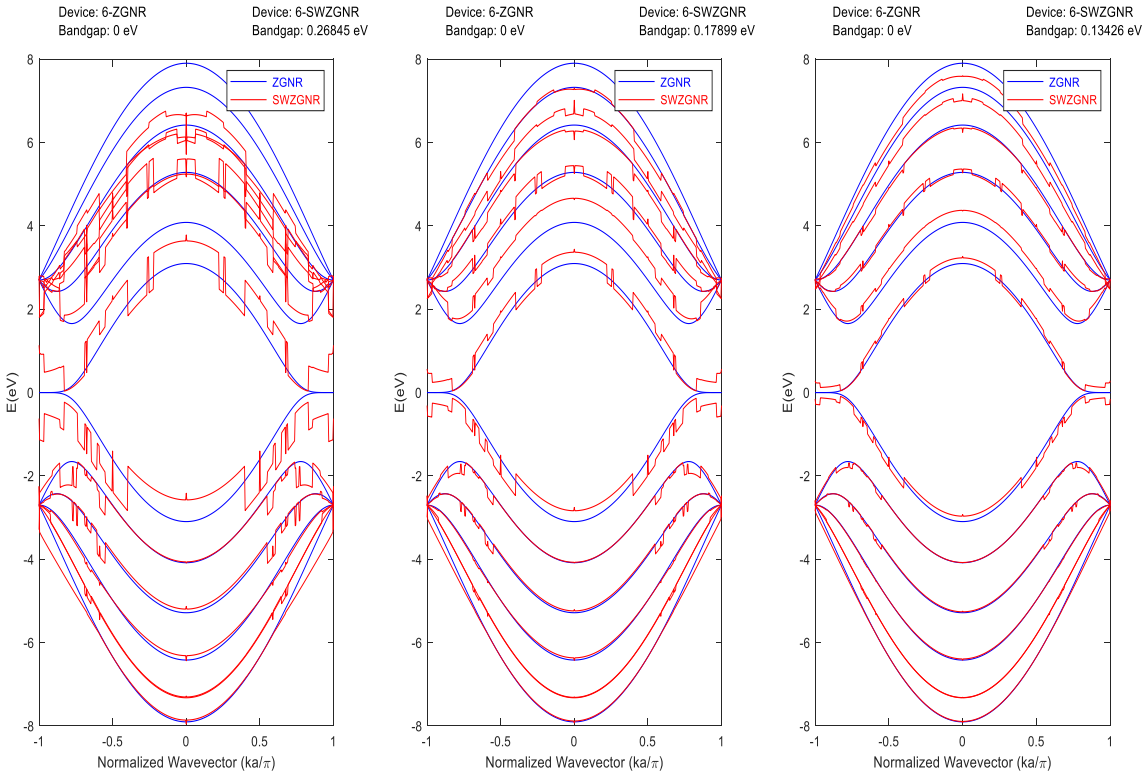

Fig. 9 Band structures of pristine ZGNRs (blue) and SWZGNRs (red) with widths of 6 and different lengths of (a) 6, (b) 12 and (c) 24 unit cells

different lengths of 11, 21 and 31. Fig. 7 shows the band structure of AGNRs (blue) and Stone-Wales defective AGNRs (red) with widths of 13 and different lengths of 11, 21 and 31. Fig. 8 shows the band structure of AGNRs (blue) and Stone-Wales defective AGNR (red) with widths of 17 and different lengths of 11, 21 and 31. The pristine AGNR subband structure shows that the bandgap value decreases as the width of the AGNR increases. Stone-Wales defective AGNR also portraits the same behaviour as the pristine AGNR in terms of bandgap trends. This can be observed by comparing the subband structures in Figs. 6, 7 and 8. The blue line represents results for the pristine AGNRs, and the red line represents results for the Stone-Wales defective AGNRs. As the width increases, the number of subbands increases. This characteristic is applied to both the AGNR and ZGNR structures.

When Stone-Wales defects are applied to the atomic structure of AGNRs, the shape of the subband structure and bandgap will change. In this study, the position of the Stone-Wales defect is always fixed at the centre of the width and centre of length because the length is an odd number, and the width is increased by 4. The blue lines and red lines do not coincide at all with the simulated subband structure results, indicating that Stone-Wales defect does affect the number of subband in the band structure. In addition, the ripple behaviour of each subband structure can also be observed in all the simulated results. This is because 90° rotation of the bond causes a change in the bond length and therefore changes the tight-binding energy. The rotation of the bonds also causes mechanical strain (Buapong and Hanlumyuang 2017) to the whole structure, which affect the subband structure since the subband structure is very sensitive to the changes in mechanical strain (Zhang *et al.* 2017). In the subband structure of Stone-Wales defective 9-AGNRs with lengths of 11, 21 and 31 as shown in Fig. 6, the red lines deviate significantly from the blue lines at length of 11. However, as the length increases, red lines gradually start to coincide with blue lines. The same patterns can also be observed in the subband structures of the Stone-Wales defective 13-AGNRs and 17-AGNRs. In addition, the Stone-Wales defective AGNRs have larger bandgaps than the pristine AGNRs. This observation agrees with the results of Chang *et al.* (2013) and Faez and Barami (2013).

4.2 Band structure of ZGNR

Fig. 9 shows the band structure of pristine ZGNRs (blue) and Stone-Wales defective ZGNR (red) with widths of 6 and different lengths of 6, 12 and 24. Fig. 10 shows the band structure of pristine ZGNRs (blue) and Stone-Wales defective ZGNR (red) with widths of 10 and different lengths of 6, 12 and 24. Fig. 11 shows the band structure of pristine ZGNRs (blue) and Stone-Wales defective ZGNRs (red) with widths of 14 and different lengths of 6, 12 and 24. Similar to AGNRs, the subband structure of ZGNRs fluctuates when Stone-Wales defects are applied to the ZGNRs.

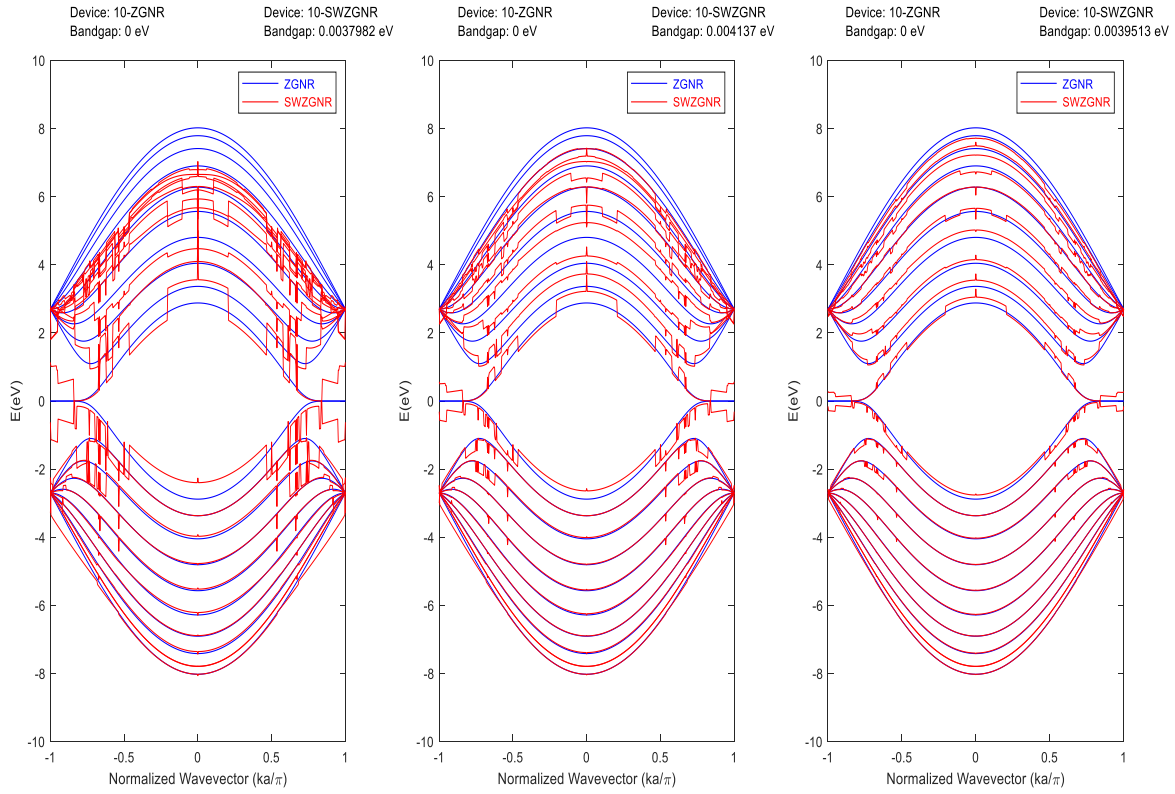

(a) (b) (c)

Fig. 10 Band structures of pristine ZGNRs (blue) and SWZGNRs (red) with widths of 10 and different lengths of (a) 6, (b) 12 and (c) 24 unit cells

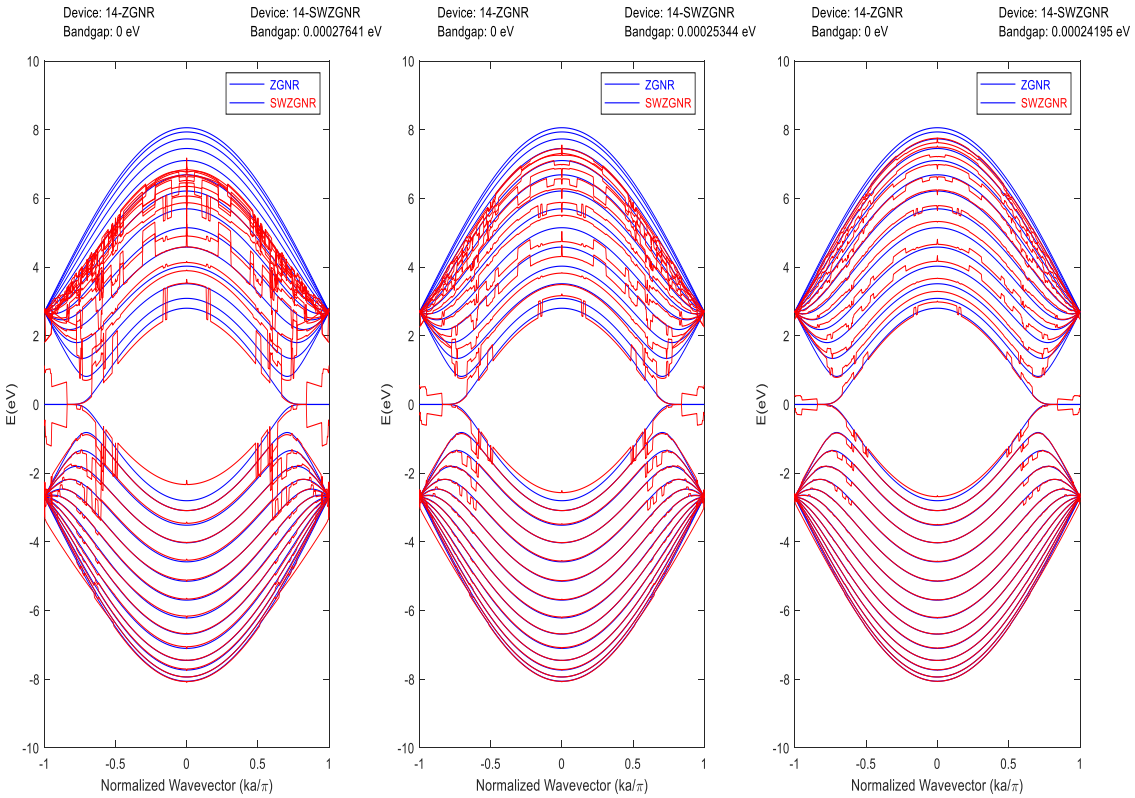

(a) (b) (c)

Fig. 11 Band structures of pristine ZGNRs (blue) and SWZGNRs (red) with widths of 14 and different lengths of (a) 6, (b) 12 and (c) 24 unit cells

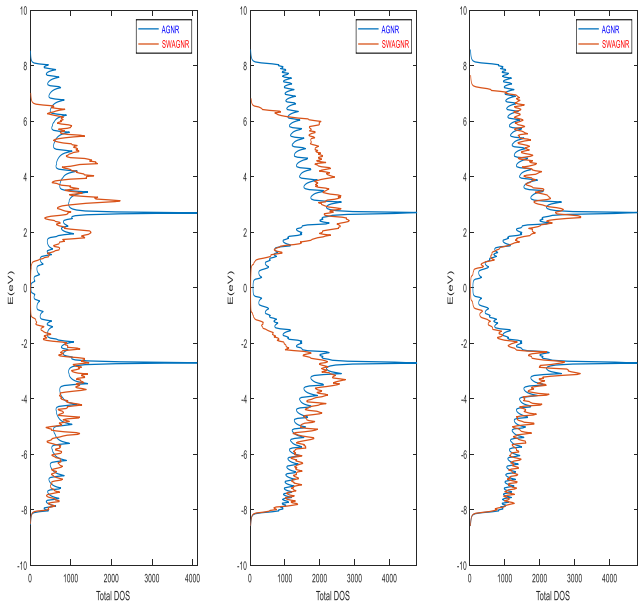

(a) (b) (c)

Fig. 12 Numerical DOS plots for (a) 21–AGNR, (b) 41–AGNR and (c) 41–AGNR with lengths of 11, 11 and 21 unit cells respectively. Blue lines represents pristine AGNRs, and red lines represent Stone-Wales defective AGNR

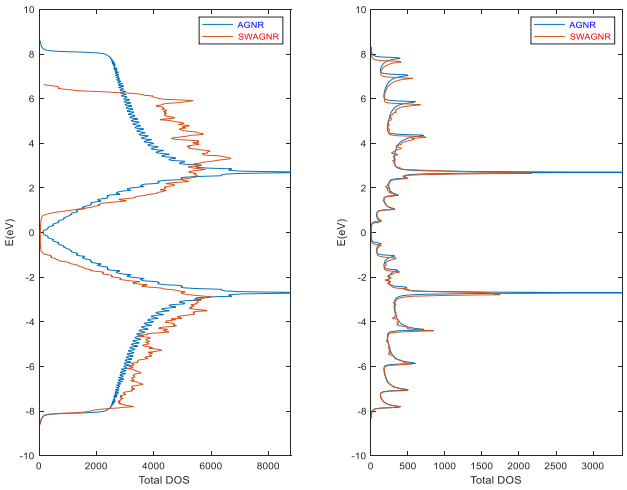

(a) (B)

Fig. 13 Numerical DOS of pristine AGNR (blue) and Stone-Wales defective AGNR (red) with (a) width of 101 and length of 11 unit cells and (b) width of 9 and length 101 unit cells

For ZGNRs, the same Stone-Wales defects are positioned at the centre of the widths and lengths. The blue lines represent the pristine ZGNR subband structures, whereas the red lines represent the defective ZGNR subband structures. Similar to AGNRs, the red lines and blue lines do not coincide with each other at every energy level, indicating that Stone-Wales defects prompted changes in subband structure of ZGNRs. This is because the tight-binding energy of -2.7 eV changes at the affected position inside the Hamiltonian matrix. As ZGNR is metallic, pristine ZGNRs have band gaps of 0 eV, but when Stone-Wales defects are applied to the structure, the band gaps increase. This is due to the negative differential resistance, which causes the ZGNR to behave like a semiconductor, as in Nguyen *et al*. (2018). The negative differential resistance is due to Van Hove singularities according to Moffatt and Kim (2006). The singularities or non-smooth points may due to the change in mechanical strain of Stone-Wales defects according to Zhang *et al*. (2017).

Nevertheless, by observing the subband structure of defective 6-ZGNRs at lengths of 6, 12 and 24, the red lines diverge from the blue lines for the defective subband structures of 6-ZGNRs when the length is 6. The subband structures of defective ZGNRs are not as smooth as pristine ZGNRs or defective AGNRs. For the sub-band structures of defective 6-ZGNRs when the length is 24, the deviation is much smaller. Similar patterns can also be observed in the subband structures of defective 10-ZGNRs and 14-ZGNRs in Figs. 10 and 11, repectively. This agrees with results of Faez and Barami (2013).

4.3 AGNR's numerical DOS

The numerical DOS is computed using Eq. (17) with the delta equation substituted into it and is applied to both AGNRs and ZGNRs. The numerical DOS using delta function is not length-dependence. Fig. 12 shows the numerical DOS of AGNRs with plots for 21–AGNRs, 41–AGNRs and 41–AGNRs with lengths of 11, 11 and 21, respectively. Fig. 13 shows the numerical DOS of AGNRs with plots for 9–AGNRs and 101–AGNRs with lengths of 101 and 11, respectively.

The results in Figs. 12 and 13 show that, by increasing the widths of the AGNRs, the Stone-Wales defective numerical DOS continues to diverge from the DOS of the pristine AGNRs. The effect of Stone-Wales defects can be reduced by increasing the length of the GNRs. This is proven by observing Fig. 13, where 9-AGNRs with a length of 101 fits quite well with pristine numerical DOS.

4.4 ZGNR's numerical DOS

The same behaviour can be observed in ZGNRs, and Fig. 14 shows the numerical DOS of ZGNRs with plots for 26–ZGNR, 42–ZGNR and 42 –ZGNR with lengths of 10, 10 and 24, respectively. Fig. 15 shows the numerical DOS of ZGNRs with plots for 6–ZGNR and 102–ZGNR with lengths of 100 and 6, respectively.

4.5 Green's function DOS of AGNRs

By using Eq. (19), Green's function DOS can be computed and plotted, as shown in Figs. 16, 17, 18 and 19. Green function's DOS contains the length information of the GNRs because the Green function's DOS is heavily affected by the Hamiltonian matrix. Any changes in the Hamiltonian matrix will affect the Green's function DOS. Fig. 16 shows the Green's function DOS of AGNRs with plots for 21–AGNRs, 41–AGNRs and 41–AGNRs with lengths of 11, 11 and 21, respectively. Fig. 17 shows the

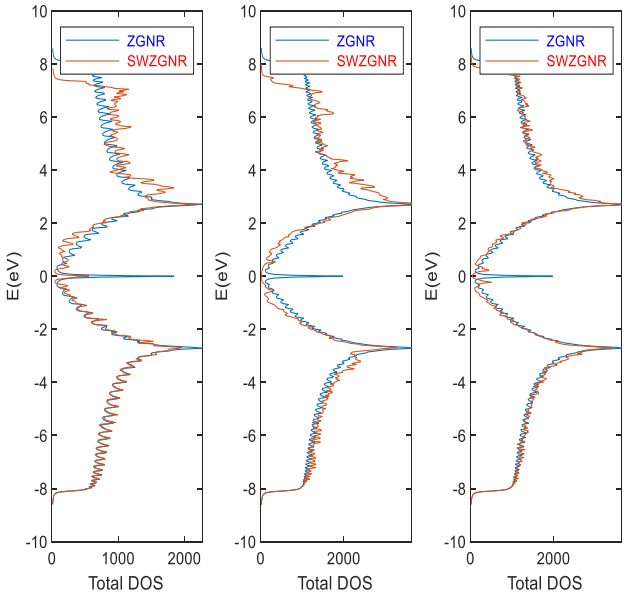

(a) (b) (c)

Fig. 14 Numerical DOS plots for (a) 26–ZGNR, (b) 42–ZGNR and (c) 42–ZGNR with lengths of 10, 10 and 24 unit cells respectively. Blue lines represent pristine ZGNRs, and red lines represent Stone-Wales defective ZGNRs

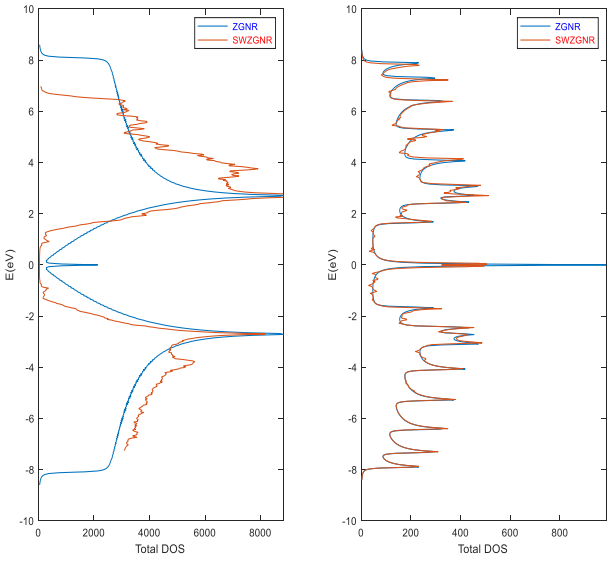

(a) (B)

Fig. 15 Numerical DOS of pristine ZGNR (blue) and Stone-Wales defective ZGNR (red) with (a) width of 102 and length of 6 unit cells and (b) width of 6 and length 100 unit cells (right)

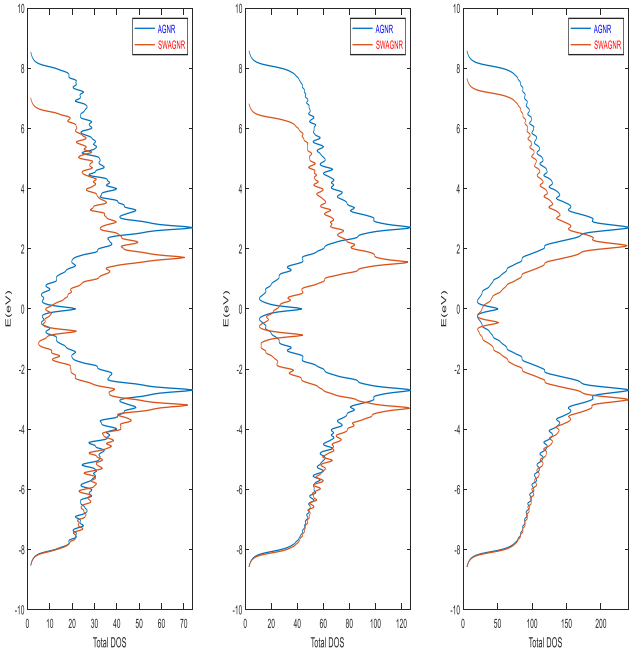

(a) (b) (c)

Fig. 16 Green's function DOS plots for (a) 21–AGNR, (b) 41–AGNR and (c) 41–AGNR with lengths of 11, 11 and 21 unit cells respectively. Blue lines represent pristine AGNRs and red lines represent Stone-Wales defective AGNRs

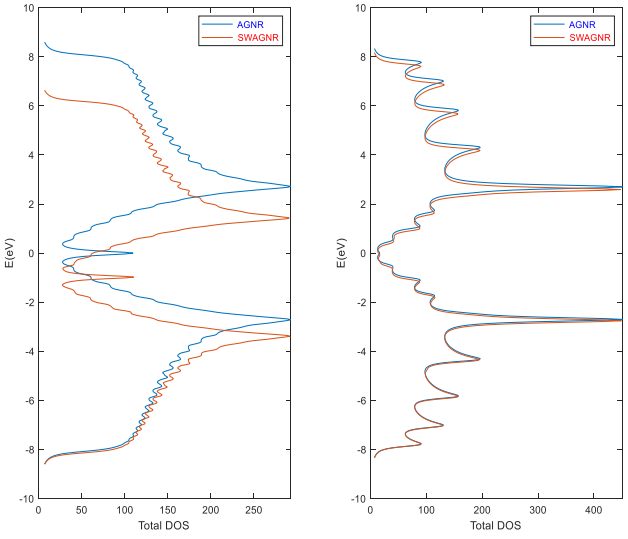

(a) (B)

Fig. 17 Green's function DOS plots for (a) 9–AGNR and (b) 101–AGNRs with length of 101 and 11 unit cells respectively. Blue lines represent pristine AGNRs and red lines represent Stone-Wales defective AGNRs.

and 101–AGNRs with lengths of 101 and 11, respectively. For all the simulated results, blue lines represent results for pristine AGNRs and red lines represent results for Stone-Wales defective AGNRs.

Comparing Figs. 16 and 17, as the width increases with a fixed length of 11, the pattern of the Green's function DOS for Stone-Wales defective AGNRs is approximately the same as that of Green's function DOS for pristine Green's function DOS of AGNRs with plots for 9–AGNRs AGNRs. However, the peaks of the Green's function DOS for Stone-Wales defective AGNRs does not coincide with the peaks of Green's function DOS of pristine AGNRs. The peaks of the Green's function DOS for pristine and defective AGNRs starts to coincide gradually only when the length increases, as observed from Figs. 16 and 17.

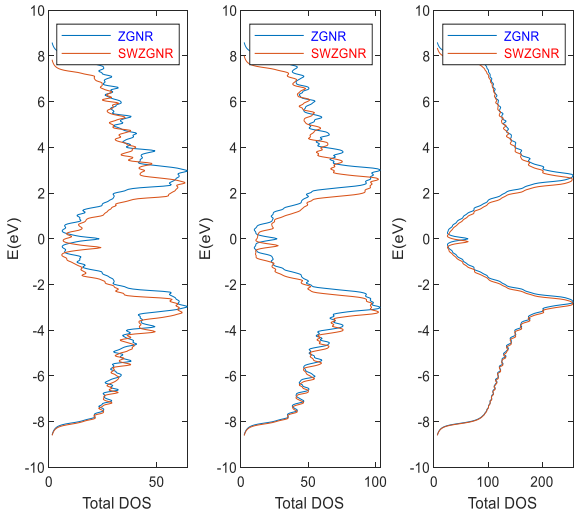

(a) (b) (c)

Fig. 18 Green's function DOS plots for (a) 26–ZGNR, (b) 42–ZGNR and (c) 42–ZGNR with lengths of 10, 10 and 24 unit cells respectively. Blue lines represent pristine ZGNRs, and red lines represent Stone-Wales defective ZGNRs

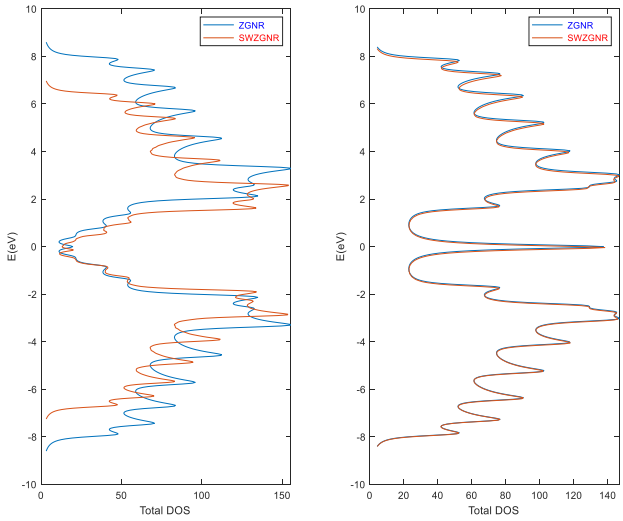

(a) (B)

Fig. 19 Green's function DOS plots for (a) 6–ZGNRs and (b) 102–ZGNRs with lengths of 100 and 6 unit cells respectively. Blue lines represent pristine ZGNRs and red lines represent Stone-Wales defective ZGNR

4.6 ZGNR's Green's Function DOS

Fig. 18 shows Green's function DOS of ZGNRs with plots for 26–ZGNRs, 42–ZGNRs and 42–ZGNRs with lengths of 10, 10 and 24, respectively. Fig. 19 shows Green's function DOS of ZGNRs with plots for 6–ZGNR and 102–ZGNR with lengths of 100 and 6, respectively. Similar behaviour occurs in ZGNRs, which is observed by comparing Figs. 18 and 19. All Green's function DOS for Stone-Wales defects have slightly lower energy, which could be due to the change in tight-binding energy when the bond length changes due to the 90° rotation of the carbon-carbon bonds in the GNRs. These changes affect the strain of the whole structure and as a result affect the electronic properties of the AGNRs and ZGNRs. In future work, the electronic properties in the present study can be further extended by modelling the carrier and current transport properties (Chuan *et al*. 2021a) for the Stone-Wales defective GNRs for further insights.

5. Conclusions

In summary, the band structure, numerical DOS and Green's function DOS of Stone-Wales-defective AGNRs and ZGNRs are simulated using the tight binding approach and MATLAB, which is numerically more efficient than the DFT method. GNR modelling is based on 3 assumptions: basic function, Hamiltonian operator discretization and plane wave approximation. The tight-binding model is created by compressing a quasi-2D GNR structure into an analogous 1D matrix system utilizing alpha and beta matrices, which represent unit cell and interunit cell connections, respectively. When a Stone-Wales defect is applied to a pristine GNR, the tight binding energies are changed due to the changing bond length at the defective bond. This causes mechanical strain on the whole structure, causing the band structure to fluctuate and increasing the bandgap of the AGNR. Pristine ZGNR had metallic characteristics, but when Stone-Wales defects were applied, the band structure showed semiconductor behaviour due to negative differential resistance, which was caused by Van Hove singularity. The values of the simulated numerical DOS and Green's function DOS decrease for both AGNR and ZGNR when the Stone-Wales defect is applied. However, when the length of the structure increases, the effect of Stone-Wales defects decreases, and the band structure and DOS coincide for both pristine and Stone-Wales defects in both AGNRs and ZGNRs. By using the results in this work, the carrier transport properties of Stone-Wales defective GNRs can be further studied in the future.

Acknowledgments

This work was supported and funded by the Ministry of Higher Education under the Fundamental Research Grant Scheme (FRGS/1/2021/STG07/UTM/02/3). The authors acknowledge the Research Management Centre (RMC), School of Graduate Studies (SPS), and Faculty of Electrical Engineering (FKE) of Universiti Teknologi Malaysia (UTM) for providing excellent support and stimulating the research environment.

References

Baggott, J. (2000), *The Meaning of Quantum Theory: A Guide For Students of Chemistry and Physics*, Oxford University Press, U.K.

Buapong, S. and Hanlumyuang, Y. (2017), "The effects of stone-

wales defect on quantum capacitance in carbon nanotube", *J. Sci. Technol. Ubon Ratchathani University*, Special Issue November 2017, 47-53.

Chang, S., Zhang, Y., Huang, Q., Wang, H. and Wang, G. (2013), "Effects of vacancy defects on graphene nanoribbon field effect transistor", *Micro Nano Lett.*, **8**(11), 816-821. http://doi.org/10.1049/mnl.2013.0457.

Chin, S.K., Lam, K.T., Seah, D. and Liang, G. (2012), "Quantum transport simulations of graphene nanoribbon devices using Dirac equation calibrated with tight-binding π-bond model", *Nanosc. Res. Lett.*, **7**(1),114. http://doi.org/10.1186/1556-276X-7-114.

Chuan, M.W., Lau, J.Y., Wong, K.L., Hamzah, A., Alias, N.E., Lim, C.S. and Tan, M.L.P. (2021a), "Low-dimensional modelling of n-type doped silicene and its carrier transport properties for nanoelectronic applications", *Adv. Nano Res.*, **10**(5), 415-422. https://doi.org/10.12989/anr.2021.10.5.415.

Chuan, M.W., Wong, K.L., Hamzah, A., Rusli, S., Alias, N.E., Lim, C.S. and Tan, M.L.P. (2021b), "Device modelling and performance analysis of two-dimensional AlSi3 ballistic nanotransistor", *Adv. Nano Res.*, **10**(1), 91-99. http://doi.org/10.12989/anr.2021.10.1.091.

Datta, S. (1997), *Electronic Transport in Mesoscopic Systems*, Cambridge University Press, Cambridge, U.K. https://doi.org/10.1017/CBO9780511805776.

Datta, S. (2002), "The non-equilibrium Green's function (NEGF) formalism: An elementary introduction", *Electr. Devices Meet.*, 7509381. https://doi.org/10.1109/iedm.2002.1175935.

Datta, S. (2005), *Quantum Transport: Atom to Transistor*, Cambridge University Press, Cambridge, U.K. https://doi.org/10.1017/CBO9781139164313.

Datta, S., Lundstrom, M., Alam, M.A. and Appenzeller, J. (2009). NCN@Purdue Summer School: Electronics from the Bottom Up, NanoHUB, Indiana, U.S.A.

Faez, R. and Barami, S. (2013), "Spin effect on band structure of zigzag and armchair graphene nanoribbones with Stone-Wales defect", *Proceedings of the 2013 21st Iranian Conference on Electrical Engineering (ICEE)*, May, 1-4. https://doi.org/10.1109/iraniancee.2013.6599606.

Goh, E., Chin, H.C., Wong, K.L., Indra, I.S.B. and Tan, M.L.P. (2018), "Modeling and simulation of the electronic properties in graphene nanoribbons of varying widths and lengths using tight-binding Hamiltonian", *J. Nanoelectr. Optoelectr.*, **13**(2), 289-300. http://doi.org/10.1166/jno.2018.2206.

Hamdi, H., Thiering, G., Bodrog, Z., Ivády, V. and Gali, A. (2020), "Stone–Wales defects in hexagonal boron nitride as ultraviolet emitters", *npj Comput. Mater.*, **6**(1), 178. https://doi.org/10.1038/s41524-020-00451-y.

Hawkins, P., Begliarbekov, M., Zivkovic, M., Strauf, S. and Search, C.P. (2012), "Quantum transport in graphene nanoribbons with realistic edges", *J. Phys. Chem. C*, **116**(34), 18382-18387. https://doi.org/10.1021/jp304676h.

Hook, T.B. (2018), "Power and technology scaling into the 5 nm node with stacked nanosheets", *Joule*, **2**(1), 1-4. https://doi.org/10.1016/j.joule.2017.10.014.

Kumar, J., Ansh and Shrivastava, M. (2020), "Stone–wales defect and vacancy-assisted enhanced atomic orbital interactions between graphene and ambient gases: A first-principles insight", *ACS Omega*, **5**(48), 31281-31288. https://doi.org/10.1021/acsomega.0c04729.

Kurban, H. and Kurban, M. (2021), "Rare-class learning over Mg-doped ZnO nanoparticles", *Chem. Phys.*, **546**, 111159. https://doi.org/10.1016/j.chemphys.2021.111159.

Kurban, H., Alaei, S. and Kurban, M. (2021a), "Effect of Mg content on electronic structure, optical and structural properties of amorphous ZnO nanoparticles: A DFTB study", *J. Non-Crystal. Solids.* **560**, 120726. https://doi.org/10.1016/j.jnoncrysol.2021.120726.

Kurban, H., Kurban, M., Sharma, P. and Dalkilic, M.M. (2021b), "Predicting atom types of anatase tio2 nanoparticles with machine learning", *Key Eng. Mater.*, **880**, 89-94. https://doi.org/10.4028/www.scientific.net/KEM.880.89.

Lee, K.H., Schnupf, U., Sumpter, B.G. and Irle, S. (2018), "Performance of density-functional tight-binding in comparison to Ab initio and first-principles methods for isomer geometries and energies of glucose epimers in vacuo and solution", *ACS Omega*, **3**(12), 16899-16915. https://doi.org/10.1021/acsomega.8b02213.

Leiserson, C.E., Thompson, N.C., Emer, J.S., Kuszmaul, B.C., Lampson, B.W., Sanchez, D. and Schardl, T.B. (2020), "There's plenty of room at the top: What will drive computer performance after Moore's law?", *Science*, **368**(6495), eaam9744. https://doi.org/10.1126/science.aam9744.

Li, T. and Lu, S.P. (2008), "Quantum conductance of graphene nanoribbons with edge defects", *Phys. Rev. B*, **77**(8), 085408. https://doi.org/10.1103/PhysRevB.77.085408.

Moffatt, P. and Kim, H.E. (2006), "Negative differential resistance from a van Hove singularity in tunnel diodes", *Appl. Phys. Lett.* **89**(19), 192117. https://doi.org/10.1063/1.2387119.

Nguyen, T.T., Bui, H.T., Nguyen, U.V. and Le, T. (2018), "Tuning electronic transport properties of zigzag graphene nanoribbons with stone-wales defect", *Commun. Phys.*, **28**(3), 201. https://doi.org/10.15625/0868-3166/28/3/12670.

Oxtoby, D.W., Gillis, H.P. and Butler, L.J. (2015), *Principles of Modern Chemistry*, Cengage learning, Boston, U.S.A.

Reich, S., Thomsen, C. and Maultzsch, J. (2008), *Carbon Nanotubes: Basic Concepts and Physical Properties*, John Wiley & Sons, Germany.

Rodrigues, J.N.B., Gonçalves, P.A.D., Rodrigues, N.F.G., Ribeiro, R.M., Lopes Dos Santos, J.M.B. and Peres, N.M.R. (2011), "Zigzag graphene nanoribbon edge reconstruction with Stone-Wales defects", *Phys. Rev. B*, **84**(15), 155435. https://doi.org/10.1103/physrevb.84.155435.

Schrödinger, E. (1926), "An undulatory theory of the mechanics of atoms and molecules", *Phys. Rev.*, **28**(6), 1049. https://doi.org/10.1103/PhysRev.28.1049.

Tang, M.S., Wang, C.Z., Chan, C.T. and Ho, K.M. (1996), "Environment-dependent tight-binding potential model", *Phys. Rev. B*, **53**(3), 979-982. https://doi.org/10.1103/physrevb.53.979.

Terrones, M., Botello-Méndez, A.R., Campos-Delgado, J., López-Urías, F., Vega-Cantú, Y.I., Rodríguez-Macías, F.J., Elías, A.L., Muñoz-Sandoval, E., Cano-Márquez, A.G. and Charlier, J.C. (2010), "Graphene and graphite nanoribbons: Morphology, properties, synthesis, defects and applications", *Nano Today*, **5**(4),351-372. https://doi.org/10.1016/j.nantod.2010.06.010.

Usuki, T., Saito, M., Takatsu, M., Kiehl, R.A. and Yokoyama, N. (1995), "Numerical analysis of ballistic-electron transport in magnetic fields by using a quantum point contact and a quantum wire", *Phys. Rev. B*, **52**(11), 8244-8255. https://dx.doi.org/10.1103/physrevb.52.8244.

Usuki, T., Takatsu, M., Kiehl, R.A. and Yokoyama, N. (1994), "Numerical analysis of electron-wave detection by a wedge-shaped point contact", *Phys. Rev. B*, **50**(11), 7615-7625. https://doi.org/10.1103/physrevb.50.7615.

Wang, C.Z., Lu, W.C., Yao, Y.X., Li, J., Yip, S. and Ho, K.M. (2008), *Tight-binding Hamiltonian from First-Principles Calculations*, Springer, Netherlands. https://doi.org/10.1007/978-1-4020-9741-6_8.

Wong, K., Chuan, M.W., Hamzah, A., Alias, N., Lim, C.S., Tan, M.L.P. and Junhuan, L. (2019), "Modeling of low-dimensional pristine and vacancy incorporated graphene nanoribbons using tight binding model and their electronic structures", *Adv. Nano Res.*, **7**(3), 209-221. http://doi.org/10.12989/anr.2019.7.3.209.

Wong, K.L., Chuan, M.W., Hamzah, A., Rusli, S., Alias, N.E., Sultan, S.M., Lim, C.S. and Tan, M.L.P. (2020), "Performance metrics of current transport in pristine graphene nanoribbon field effect transistors using recursive non-equilibrium Green's function approach", *Superlatt. Microstruct*., **145**, 106624. https://doi.org/10.1016/j.spmi.2020.106624.

Zhang, W., Yin, J., Zhang, P. and Ding, Y. (2017), "Strain/stress engineering on the mechanical and electronic properties of phosphorene nanosheets and nanotubes", *RSC Adv*., **7**(81), 51466-51474. https://doi.org/10.1039/c7ra09668b.

Zhang, X., Wu, T., Jiang, Q., Wang, H., Zhu, H., Chen, Z., Jiang, R., Niu, T., Li, Z., Zhang, Y., Qiu, Z., Yu, G., Li, A., Qiao, S., Wang, H., Yu, Q. and Xie, X. (2019), "Single-crystal graphene wafers: Epitaxial growth of 6 in. single-crystalline graphene on a Cu/Ni (111) film at 750 °C via chemical vapor deposition", *Small*, **15**(22), 1970120. https://doi.org/10.1002/smll.201970120.

AT